1990-01-15

Forecasting Bering Sea ice edge behavior

Pritchard, R.S.; Mueller, A.C.; Yang, Y.S.; Hanzlick, D.J.

Journal Name: Journal of Geophysical Research; (United States); Journal Volume: 95:C1
http://hdl.handle.net/10945/61059

JOURNAL OF GEOPHYSICAL RESEARCH, VOL. 95, NO. C1, PAGES 775–788, JANUARY 15, 1990

Forecasting Bering Sea Ice Edge Behavior

R. S. PRITCHARD,[1,2] A. C. MUELLER,[3] D. J. HANZLICK,[4] AND Y.-S. YANG[5]

A coupled ice/ocean dynamics model is developed to provide Arctic offshore operators with 5- to 7-day forecasts of ice motions, ice conditions, and ice edge motions. An adaptive grid is introduced to follow the ice edge, and the grid may move independently of the ice motion. The grid can be Lagrangian or Eulerian at different locations away from the ice edge. Ice stress is described using an elastic-plastic model with strength determined by the ice conditions. The ocean dynamics model describes time-dependent, three-dimensional behavior, including wind-driven currents and barotropic and baroclinic flows. The thermal energy budget of the ice cover is coupled to the ocean, with mass and salt interchange accompanying freezing or melting. Near the marginal ice zone (MIZ), surface winds (determined by reducing and turning the geostrophic winds) are enhanced to reflect observed behavior. The model was tested by simulating ice edge motions observed during the 1983 Marginal Ice Zone Experiment-West and during drilling of the 1983 north Aleutian shelf Continental Offshore Stratigraphic Test well. Simulations of ice edge movement in the Bering Sea compare with observed data to within about 5 km/d. The model correctly describes mixed-layer evolution in the marginal ice zone as fresh meltwater is mixed downward by turbulence. Along-edge baroclinic flows due to density gradients across the ice edge are simulated by the model, in agreement with observations. Increased ice drift speeds generate higher melt rates due to increased turbulence levels, with the result that ice edge advance is moderated in spite of higher ice drift speeds.

1. INTRODUCTION

Drilling operations in the Bering Sea now use drill rigs designed for use in temperate waters. The rigs are not designed to withstand sea ice forces, so that operators must stop drilling and leave the site if ice approaches too near. Present-day drilling operations continue only while the sea ice is far away, say 150 km. During this early exploration phase in the Bering Sea, only one or two wells are drilled by a single rig during the ice-free season, and if forced to leave a site, the rig generally leaves for the season. But even with these restrictions, there is a possibility of sea ice approaching dangerously near, as happened during drilling of a north Aleutian shelf Continental Offshore Stratigraphic Test (COST) well [*Grittner et al.*, 1983]. The need to keep drill rigs on site near the ice edge for as long as possible suggests that a useful ice model must describe ice conditions near the ice edge and must resolve ice edge location to within about 5 km.

The ice edge motion model has been developed to help these operations by providing forecasts of ice behavior 5–7 days ahead. The model allows forecasting of ice edge behavior, while at the same time it increases our understanding of the physical processes affecting the ice. Other systems of environmental monitoring and forecasting have been developed for the Beaufort Sea [*Dixit et al.*, 1984; *Eley*, 1986; *Steen and Trobak*, 1986], but the ice edge model presented here is the first to couple an ice dynamics model with a three-dimensional ocean dynamics model where both models contain sophisticated descriptions of the physical processes that control sea ice and ocean surface behavior. We identified the essential physical processes and included their effects on the force and thermal energy balance of the ice and ocean. As a result, the model can simulate the ice and ocean behavior under a wide variety of weather, ice, and ocean conditions. Material parameters in the model are all set to standard values given in the literature cited, except when stated. These nominal values are not adjusted to improve model performance.

The forecast model is driven by weather forecasts supplied by an outside source (e.g., NOAA/Navy Oceanographic Data Distribution Service (NODDS) or National Weather Service (NWS)). The model requires that the present ice and ocean conditions be specified as initial conditions. The model can forecast motions of the ice cover, and changes in ice conditions, ice edge location, ocean currents, salinity, temperature, and density fields. Since inertia terms are included in both the ice and ocean dynamics models, it is possible to describe tidal and inertial effects if appropriate boundary and initial conditions are used. The simulations presented here, however, describe daily average behavior and do not include these effects.

Results of two simulations are presented to verify model performance. The first study simulated a period in February 1983, during the Marginal Ice Zone Experiment (MIZEX) West program, which focused on the ice edge behavior in the central Bering Sea. The second study simulated a period in January 1983, during drilling of the north Aleutian shelf COST well near Port Moller, when the ice edge advanced rapidly, nearly overrunning the site. These time periods were selected because of the comprehensive data available and because observed behavior of the ice was interesting and different for the two periods.

2. BERING SEA CONDITIONS

Ice usually begins to form in the northern Bering Sea in October and continues to move and grow southward, reaching its greatest extent in March or April [*Walsh and Johnson*, 1979]. The ice thickness is generally 0.5–2.0 m [*Niebauer*, 1980], with 1 m being typical. Springtime retreat is rapid, and the Bering Sea may be ice free by June or July [*LaBelle et al.*, 1983]. The southern limit of ice extent is controlled by

[1]Naval Postgraduate School, Monterey, California.
[2]Permanently at IceCasting, Inc., Seattle, Washington.
[3]Flow Industries, Inc., Kent, Washington.
[4]Seattle, Washington.
[5]Arco Oil and Gas Company, Dallas, Texas.

Paper number 89JC01568.
0148-0227/90/89JC-01568$05.00

the heat content of deeper water. Over long time periods, the ice edge tends to extend no farther south than the shelf break [*Overland and Pease*, 1982]. On shorter time scales, as the ice drifts southward into warmer water, cold meltwater is produced at the ice edge, which reduces further melting and enables the ice edge to proceed farther southward [*Pease*, 1981].

The large-scale circulation of the Bering Sea is dominated by a cyclonic gyre over the deep basin [*Hughes et al.*, 1974; *Takenouti and Ohtani*, 1974]. Mean flow over the Bering Sea shelf is to the north or northwest toward the Bering Strait with a total transport of about 1 Sv. This flow is confined to the shelf and is only weakly coupled to the main gyre. *Coachman and Aagaard* [1981] indicated that large-scale meteorological events could temporarily interrupt this pattern but the mean would remain sluggishly northward. Speeds over the outer shelf and slope regions are of the order of 10 cm/s. While there is some doubt whether or not flow into the Bering Sea through the central and eastern passages of the Aleutian chain is significant [*Kinder and Schumacher*, 1981], Pacific water does appear to enter through Near Strait, and there appears to be outflow through Kamchatka Strait [*Hughes et al.*, 1974]. Quantitatively, this water balance involves the exchange of about 25–35 Sv.

During winter, when sea ice poses a threat to drilling operations, cold northeasterly winds, resulting from the seasonal establishment of the Siberian high and the Aleutian low, typically prevail over much of the Bering Sea. These conditions have been described as a "conveyor belt" [*Muench and Ahlnas*, 1976; *Pease*, 1980] in which ice forms in the north, moves southward at an average speed of about 25 cm/s, and melts at the southern ice edge. As the young ice moves away from the lee shores in Bristol Bay and the northern Bering Sea, the water is cooled by the atmosphere, thereby ensuring continued ice production. In areas of active ice production, brine rejection occurs, and the resulting density changes drive vertical convection and mixing, which helps deepen the cold surface layer and depresses the freezing temperature of the water. However, the eastward passage of cyclones adds variability to the wind field [*Overland and Pease*, 1982]. Ice has been observed to drift north and south over distances of 100–200 km in 10- to 20-day time periods [*Pease and Salo*, 1987; *Pritchard*, 1988].

Large ice floes are driven southwestward by the wind, and as they approach the ice edge, ocean swells fracture them, and they raft and ridge [*Martin and Bauer*, 1981]. The ice tends to be compact when winds are on-ice, with floes herded together by the wind and incoming ocean wave energy, but when winds are off-ice, floes at the edge can move away from the pack, forming streaks and bands. During March 1981, a 20% increase in wind speed from 90 km inside the ice edge to 90 km seaward was observed [*Reynolds*, 1984]. It was accompanied by a temperature increase from −11 to −5°C, and the boundary layer height increased from 450 to 600 m over the ocean. *Overland et al.* [1983] suggested that the increased wind explained the observed ice accelerations in the MIZ.

As the ice disperses, the ocean surface is exposed to the air, changing the thermal heat budget and the force balance. The atmospheric boundary layer thins, form drag on the ice sails increases, wave radiation in the water between the floes increases, water drag decreases from fresh meltwater, air stress acts directly on the water, and velocity of surface water between the floes changes. The increased roughness leads to greater coupling with the wind, and the floes move away from the pack farther southward into warmer water until they disintegrate. The fresh meltwater is mixed throughout the mixed layer by turbulence [*McPhee*, 1983; *Josberger*, 1983; *Muench and Schumacher*, 1985]. Depth of the mixed layer is regulated by the ratio of turbulent kinetic energy to buoyancy potential energy, which depend on gradients of velocity and density, respectively. Since turbulent kinetic energy decays with depth, there is a depth below which it is small relative to the buoyancy potential energy, which prevents turbulence from mixing further downward. Water below the mixed layer is unchanged, remaining more saline, warmer, and slower moving. The fresh meltwater at the surface and its stable density gradient enable the pycnocline to persist as a two-layer system. *McPhee* [1983] modeled turbulent heat and momentum transfer under melting ice and found that melting depends on stress at the interface, the effective ice/water drag is decreased at ocean temperatures observed in the MIZ, and this drag reduction could account for the seaward acceleration of ice in the MIZ. *Muench and Schumacher* [1985] reported that melting at the ice edge produced a horizontal density gradient that caused a northwestward baroclinic current, parallel to the ice edge with near-surface speeds of 5–6 cm/s. The baroclinic flow supplements an along-isobath barotropic flow to yield a total northwestward near-surface flow with monthly mean speeds exceeding 10 cm/s.

3. Ice Model

3.1. *Mass Balance*

Ice conditions are represented by the thickness distribution $G(\mathbf{x}, h, t)$, the fraction of area in the neighborhood of point $\mathbf{x}$ covered by ice thinner than h. Compactness $A(\mathbf{x}, t)$ is

$$A = 1 - G(\mathbf{x}, 0^+, t) \tag{1}$$

where $G(\mathbf{x}, 0^+, t)$ is the fraction of open water (the notation 0^+ represents the limit as $h \to 0$). Changes in thickness distribution arise from both thermal growth and mechanical redistribution [*Thorndike et al.*, 1975]:

$$DG/Dt + F\,\partial G/\partial h = \Psi - G\nabla \cdot \mathbf{v} \tag{2}$$

where DG/Dt is the substantial derivative, $F(\mathbf{x}, h, t)$ is the rate of change of thickness of ice in thickness category h, Ψ is the rate of production of thicker ice from thinner ice as rafting and ridging occur and also the rate of production of open water as the ice deforms, and $G\nabla\cdot\mathbf{v}$ is caused by the rate of area change. The gradient operator ∇ describes two horizontal components.

In the Bering Sea, redistribution due to rafting and ridging is generally small. Changes in ice conditions are usually dominated by thermal growth or melt and by formation of open water as the ice cover diverges. Ice growth rates F, for each thickness category, are derived from the thermal energy balance equation. The redistribution function Ψ depends on G and the plastic stretching $\mathbf{D}_p$, following the concepts introduced by *Thorndike et al.* [1975]. It is a linear function of the stretching magnitude, which makes the response rate-independent, and is therefore consistent with the plasticity constitutive law.

3.2. *Momentum Balance*

Ice velocity $\mathbf{v}(\mathbf{x}, t)$ and all other vectors in the model (both ice and ocean) are limited to two horizontal components. The forces acting on the ice cover include air stress, water stress, internal ice stress divergence, sea surface tilt, and Coriolis and inertial accelerations:

$$m(D\mathbf{v}/Dt + f\mathbf{k} \times \mathbf{v} + g\nabla\eta) = A(\boldsymbol{\tau}_{ai} + \boldsymbol{\tau}_{wi}) + \nabla \cdot \boldsymbol{\sigma} \quad (3)$$

where m is mass per unit area of ice, f is the Coriolis parameter, g is the gravitational constant, η is sea surface elevation, $\boldsymbol{\tau}_{ai}$ is air stress, $\boldsymbol{\tau}_{wi}$ is water stress, and $\boldsymbol{\sigma}$ is internal ice stress (more accurately, it is the ice stress integrated through the ice thickness in excess of isostatic equilibrium).

The areal ice density $m = \rho_i H$ is ice density ρ_i times mean ice thickness H:

$$H = \int h \, dG \quad (4)$$

Although the sea surface slope term is an order of magnitude smaller than other terms in the momentum balance, it must be included to allow the ice to drift with the surface currents in the absence of winds. For time periods greater than 1 day, the inertia is negligible, but it is included to describe tidal and inertial behavior if desired.

3.3. *Stress-Deformation Constitutive Law*

When the applied loads are small, sea ice resists horizontal compression, but as loads increase, the ice rafts and ridges. Alternately, if the forces cause divergence of the ice cover, leads form, and the ice floes become surrounded by interstitial water. Ice is generally thought to have a negligible tensile strength and to resist compression only when compactness exceeds about 80% [*Coon et al.*, 1974; *Hibler*, 1985]. For the most part, ice in the southern Bering Sea that is near to the ice edge and far from shore drifts without a strong influence of internal ice stress. However, when the ice is driven northward, compacting it, and in regions like Bristol Bay where ice is within 50 km of shore, ice stress can influence its behavior. It is difficult to decide a priori when ice stress is important. Fortunately, plasticity can describe whether or not ice stress is significant, and so we have included an ice constitutive law in the model at all times, allowing the constitutive law to determine when the ice stress is significant.

The elastic-plastic constitutive law [*Pritchard*, 1975, 1981] is composed of four elements: yield constraint, flow rule, elastic response, and kinematic relationship, with ice strength determined as a function of the ice conditions. *Kollé and Pritchard* [1983] have shown that this ice dynamics model can simulate Beaufort Sea ice motions to within 3 km/d.

The isotropic yield constraint is

$$\phi(\sigma_{\mathrm{I}}, \sigma_{\mathrm{II}}, p^*) \leq 0 \quad (5)$$

where $\sigma_{\mathrm{I}} = \frac{1}{2}\,\mathrm{tr}\,\boldsymbol{\sigma}$ is the average stress (negative of pressure), $\sigma_{\mathrm{II}} = (\frac{1}{2}\,\mathrm{tr}\,\boldsymbol{\sigma}'\boldsymbol{\sigma}')^{1/2}$ is the shear stress magnitude, $\boldsymbol{\sigma}' = \boldsymbol{\sigma} - \sigma_{\mathrm{I}}\mathbf{I}$ is the deviatoric stress tensor, and p^* is isotropic compressive strength. A diamond-shaped surface is used (as viewed in this principal stress space). For this yield surface, tensile stresses are prohibited, and compressive stresses are limited so that $-\sigma_{\mathrm{I}} + \sigma_{\mathrm{II}} \leq p^*$. Strength is estimated by equating work done by the stresses during deformations to the sum of work done by gravitational forces as the ice blocks are piled into rafts and ridges, work done by Coulomb friction as blocks slide into rubble [*Rothrock*, 1975], and work done by shearing that causes no large-scale redistribution of ice [*Pritchard*, 1981] resulting in

$$p^* = c^* \int h^2 a(h) \, dh \quad (6)$$

where $a(h)$ is the fraction of ice participating in the redistribution process (it is defined by the redistribution function Ψ) and c^* depends on density and ice friction coefficients. All material constants in the ice dynamics model, including the expression for c^*, are taken from *Pritchard* [1981].

An associated flow rule describes plastic stretching $\mathbf{D}_p$

$$\mathbf{D}_p = \lambda \, \partial\phi/\partial\boldsymbol{\sigma} \quad (7)$$

where λ is a nonnegative scalar multiplier that keeps stress on the yield surface.

The stress satisfies an isotropic linear elastic response,

$$\boldsymbol{\sigma} = (M_1 - M_2)\mathbf{I}\,\mathrm{tr}\,\mathbf{e} + 2M_2\mathbf{e} \quad (8)$$

where M_1 and M_2 are bulk and shear moduli, respectively, and $\mathbf{e}$ is elastic strain.

Finally, elastic strain is related to the stretching $\mathbf{D}$ by

$$D\mathbf{e}/Dt - \mathbf{We} + \mathbf{eW} = \mathbf{D} - \mathbf{D}_p \quad (9)$$

where $\mathbf{D}$ is stretching (velocity strain) and $\mathbf{W}$ is spin (vorticity).

3.4. *Thermal Energy Balance*

Ice growth rates satisfy a quasi steady state model with linear vertical temperature profile, no horizontal heat diffusion, and zero heat capacity. Snow cover has not been included in the model. Over periods of 5–7 days, the effect should not be too large. These assumptions are reasonable for thin Bering Sea ice ($h < 0.8$ m). The model and all parameter values follow *Maykut* [1978, 1982].

When the upper ice surface temperature T_0 is below the freezing point of the ice, heat flux balance satisfies

$$(1 - \alpha)Q_r - Q_p + Q_l - Q_o + Q_s + Q_e + Q_c = 0 \quad (10)$$

where α is albedo, Q_r is incident shortwave radiation, Q_p is penetrating heat flux (depends on Q_r, albedo and thickness), Q_l is incoming longwave radiation, Q_o is outgoing longwave radiation (proportional to the fourth power of T_0), Q_s is sensible heat flux (proportional to $T_a - T_0$, the difference between the atmosphere and ice temperatures), Q_e is evaporative heat flux (depends on the relative humidity, barometric pressure, and the saturation pressures at the atmosphere and ice temperatures), and Q_c is conductive heat flux (proportional to the temperature difference across the ice). The barometric pressure, air temperature, relative humidity, surface wind speed, and cloud cover are input from the atmospheric model. The incident shortwave and longwave radiation and evaporative heat flux follow *Zillman* [1972]. If the solution to (10) gives an estimate of T_0 that is below the

freezing point, then the ice growth rate F on the bottom surface satisfies the Stefan condition

$$\rho_i L_f F = Q_c - Q_w \tag{11}$$

where ρ_i is ice density, L_f is latent heat of fusion, and Q_w is oceanic heat flux. The oceanic heat flux Q_w is described in section 6.2, equation (42). If the solution to (10) gives an estimate of T_0 that is above the freezing point, then T_0 is set equal to the freezing temperature, and ice growth rate is determined from the atmospheric and oceanic heat fluxes

$$\rho_i L_f F = (1 - \alpha)Q_r - Q_p + Q_l - Q_o + Q_s + Q_e - Q_w \tag{12}$$

The flux of salt rejected by the growing ice is approximated by

$$F_s = 10^{-3}\rho_i F(1 - k)S \tag{13}$$

where $k(h)$ is fraction of salt incorporated in ice during growth and S is ocean salinity. Melting of ice provides fresh water, for which $k = 0$.

4. Ice Edge Behavior

An adaptive grid is introduced to describe ice behavior. Since this grid is designed to follow the motion of the ice edge, it is presented together with the ice edge behavior in this section. The motion of this grid may be selected by the user independently of the motion of the ice, an approach that allows one grid line to follow the motion of the ice edge, while other grid lines follow ice floes, and still others remain stationary. This approach generalizes the classical descriptions in which ice velocity, ice conditions, and other properties are described using either a Lagrangian or an Eulerian grid.

In the Lagrangian description (usually used in solid mechanics), the ice floes are identified, and their motions are followed, which gives good resolution because the motion of each particle is followed explicitly and there is no numerical dispersion of ice across the grid lines. However, if large shearing occurs, numerical solutions become inaccurate. Also, the ice edge cannot be treated as a Lagrangian line because melting (freezing) moves the line relative to the floes. In the Eulerian description (usually used in fluid mechanics), fixed positions in space are identified, and motion of ice floes through the grid is followed. This approach is good when severe deformations occur because the grid is not deformed, but ice within a cell at each time step is diffused throughout that cell, and there is no way to identify the position of a particle to within less than the cell size. An Eulerian description requires that a large number of cells be maintained near the ice edge and beyond, to cover the region into which ice might drift.

Although motion of each point on the adaptive grid may be specified independently, the advantages of the adaptive grid are realized when the grid velocity field is specified in some logical manner dependent on the ice behavior. The essential step is to choose the ice grid so its boundary follows the ice edge. This feature eliminates numerical dispersion across the ice edge. Furthermore, where gradients are expected to be large, the grid should have fine resolution and follow the gradient, and where gradients are expected to be small, the grid should spread out to save computational time and costs.

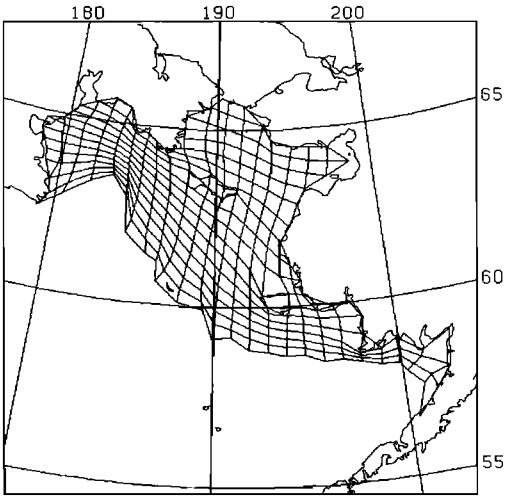

Fig. 1. Ice model grid.

At these points, its motion is not important. Some grid points may be chosen to be Lagrangian, others Eulerian, with the restriction that grid velocity must vary smoothly throughout the domain. As we have already stated, along the ice edge, grid points move with the ice edge velocity. Along coastlines, the grid may be stationary or slide along the shore. Around islands, the grid is stationary. These choices eliminate mangled grids. Finally, the interior points move by Laplacian grid generation [*Thompson*, 1982] with forcing terms that maintain a refined grid at the edge. In addition to allowing a rather arbitrary grid velocity field, the model also allows the operator to introduce a rather arbitrary initial grid. The analyst can minimize detail away from the ice edge or other areas of little interest by using large grid cells. When dispersed ice conditions occur, the numerical grid adapts to capture the streaks and bands within the last row of cells. A sample grid is shown in Figure 1, where one grid line lies along the ice edge and the spacing is closer near the ice edge.

4.1. *Referential Description*

The reference configuration (it is reasonable to think of it interchangeably as the numerical grid) has a smooth velocity field $\mathbf{w}$. The motion of the reference configuration is defined by its velocity field $\mathbf{w}$, which may be specified independently of the ice motion. Both the temporal and spatial variations may be chosen by the user. In the referential description, the time rate of change of each solution variable Ψ (e.g., velocity, stress, or temperature) is the value Ψ' seen by an observer moving with the reference configuration. If $D\Psi/Dt$ is the substantial derivative (the rate of change seen by an observer moving with the ice floes), the two derivatives are related by

$$\Psi' = D\Psi/Dt + (\mathbf{w} - \mathbf{v}) \cdot \nabla\Psi \tag{14}$$

where $\mathbf{w}$ is the local velocity of the arbitrary reference configuration and $\mathbf{v}$ is the ice velocity. Where the reference configuration is Lagrangian, $\mathbf{w} = \mathbf{v}$, advection is zero, and the time derivative in the reference configuration equals the material derivative $\Psi' = D\Psi/Dt$. Where the reference configuration is Eulerian, $\mathbf{w} = \mathbf{0}$, and the time derivative in the reference configuration equals the partial time derivative

$\Psi' = \partial\Psi/\partial t$. Equation (14) is then the familiar relationship between the substantial derivative and the partial time derivative $D\Psi/Dt = \partial\Psi/\partial t + \mathbf{v}\cdot\nabla\Psi$, except that the advection term has been moved to the other side of the equation.

4.2. *Ice Edge Motion*

The ice edge is defined to be the northernmost line along which the ice has zero compactness. An accurate forecast of the position of this line can help describe the region where drilling operations can proceed in ice-free safety. Actually, it is not necessary to follow every wiggle in the ice edge because the thickness distribution can describe areas within the domain (ice grid) that are ice-free. In practice, a smooth ice edge curve is introduced initially, with the constraint that ice cannot extend beyond it, but regions of zero compactness are allowed to appear within the ice grid.

The ice edge is defined as the curve along which ice compactness is zero:

$$A(\mathbf{x}_e, t) = 0 \tag{15}$$

where $\mathbf{x}_e$ is the set of locations at time t lying along the edge curve. Locations along the edge curve $\mathbf{x}_e$ may be parameterized in terms of s, the distance along the edge curve

$$\mathbf{x}_e = \Gamma(s, t) \tag{16}$$

where Γ describes the ice edge curve.

The ice edge moves as ice floes near the edge drift, and it also moves relative to these floes as they melt. Motion of the edge curve is determined by considering variations in (15). Since both s and t are independent

$$\delta A = [\nabla A \cdot \partial\mathbf{x}_e/\partial s]\delta s + [\nabla A \cdot \partial\mathbf{x}_e/\partial t + \partial A/\partial t]\delta t \tag{17}$$

where all rates of change must be considered as Eulerian rates because (15) is expressed in terms of instantaneous spatial position and time. Since A is zero everywhere along the edge curve, the variations $\delta A \equiv 0$ also for all variations δs and δt. Therefore each of the bracketed coefficients must be zero everywhere along the edge curve. If $\mathbf{n}$ is a unit outward normal vector to the edge curve, its components satisfy $n_x = \partial y_e/\partial s$ and $n_y = -\partial x_e/\partial s$, and the first bracketed coefficient is written $-\partial A/\partial x\, n_y + \partial A/\partial y\, n_x = 0$, which in vector notation is $\mathbf{n} \times \nabla A = \mathbf{0}$. The zero cross product between $\mathbf{n}$ and the compactness gradient implies that ∇A is parallel to $\mathbf{n}$. This result simply confirms our mathematics because the derivative of the zero compactness function along the edge curve must be zero. Setting the second bracketed term to zero and rewriting in vector notation give

$$\nabla A \cdot \partial\mathbf{x}_e/\partial t + \partial A/\partial t = 0 \tag{18}$$

which allows us to determine velocity of the edge curve $\partial\mathbf{x}_e/\partial t$ at each location in terms of the compactness gradient ∇A and temporal change $\partial A/\partial t$. The time rate of change of compactness is expressed in terms of the material rate DA/Dt, which can be determined from the thickness distribution model ((1) and (2)). The substantial derivative is $DA/Dt = \partial A/\partial t + \nabla A\cdot\mathbf{v}$ and upon substitution (18) becomes

$$\nabla A \cdot [\partial x_e/\partial t - \mathbf{v}] + DA/Dt = 0 \tag{19}$$

Since the component of ∇A parallel to the edge curve is always zero, (19) is affected only by the component orthogonal to the edge curve (parallel to $\mathbf{n}$), and therefore only the normal component of the relative velocity can be determined. The normal component of the relative velocity

$$(\partial\mathbf{x}_e/\partial t - \mathbf{v}) \cdot \mathbf{n} = -M \tag{20}$$

where M is the rate of meltback at the ice edge due to thermal effects. The meltback rate is

$$M = (DA/Dt)/(\mathbf{n} \cdot \nabla A) \tag{21}$$

where the normal component of the compactness gradient has been shown explicitly.

The material rate of change of compactness DA/Dt is evaluated by differentiating (1) and substituting the result into (2) evaluated for the fraction of open water. The equation governing compactness becomes

$$DA/Dt = (F\ \partial G/\partial h)_{h=0} \tag{22}$$

where the effects of mechanical redistribution have been neglected by assuming that enough open water exists to absorb all deformations. Under these conditions, $\Psi(\mathbf{x}_e, 0^+, t) = 0$, and the meltback rate is

$$M = (F\ \partial G/\partial h)_{h=0}/\mathbf{n} \cdot \nabla A \tag{23}$$

which is a function of the rate of change of thickness of infinitesimally thin ice $F(0)$, the fraction of area covered by the infinitesimally thin ice $\partial G/\partial h(0)$, and the compactness gradient ∇A.

It is important to remember that (18)–(23) are simply restatements in incremental form that the edge curve lies along a set of points where compactness is zero. This relationship is useful when considering edge motion when the ice floes at the edge melt and compactness is not uniform ($\nabla A \neq 0$).

4.3. *Ice Grid Motion*

When the ice edge velocity is well defined and bounded, the ice grid lying along the initial ice edge is assigned a velocity equal to the ice edge velocity. This line then follows the ice edge for all time. If a finite region melts instantaneously because compactness was uniform, the unbounded velocity is handled numerically by moving the grid in one time step, and the singularity is circumvented. A similar problem occurs during freezing conditions (a less frequent, but important condition for drilling operators), when a finite region freezes simultaneously. In this case we resort to the original nonincremental formulation. The ice edge is defined to lie along the freezing isotherm of the sea surface temperature, which is determined from the ocean temperature field. Although the ice edge moves a finite distance instantaneously, the thickness distribution can be modified to account for the zero thickness ice that was advected into the ice domain.

The ice grid velocity along the ice edge could be set equal to the ice edge velocity $\mathbf{w} = \partial\mathbf{x}_e/\partial t$, but since only the velocity component orthogonal to the ice edge affects (18), this definition would require that the grid velocity parallel to the ice edge be set equal to the ice drift velocity separately. This definition, however, can accentuate distortion of the grid in regions where the edge curve meanders a lot. We eliminate this potential problem by choosing the grid velocity to be orthogonal to the ice edge (Figure 2):

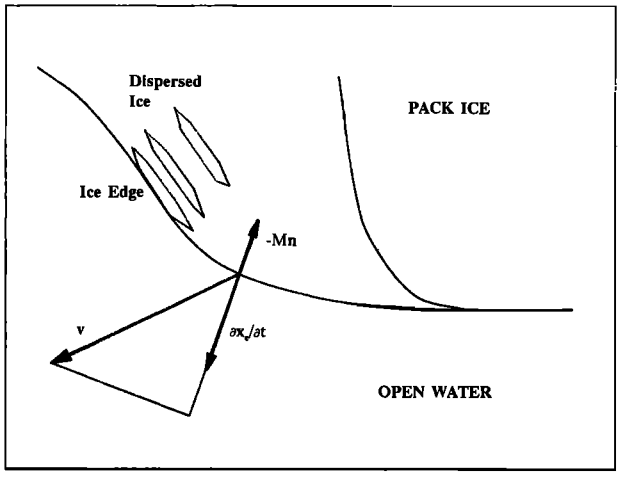

Fig. 2. Ice edge velocity definition.

$$\mathbf{w} = (\mathbf{v} \cdot \mathbf{n} - M)\mathbf{n} \tag{24}$$

This definition allows the grid to slide along the ice edge, which helps to maintain a more uniform interior grid.

5. Ocean Model

The ocean dynamics model describes the time-dependent, three-dimensional behavior of the horizontal current velocity $\mathbf{u}(z, \mathbf{x}, t)$, vertical current $w(z, \mathbf{x}, t)$, pressure $p(z, \mathbf{x}, t)$, sea surface elevation $\eta(\mathbf{x}, t)$, temperature $T(z, \mathbf{x}, t)$, and salinity $S(z, \mathbf{x}, t)$, where z is depth and $\mathbf{x}$ is horizontal position. Momentum balance is derived from the three-dimensional Navier-Stokes equations with the usual Boussinesq assumption,

$$D\mathbf{u}/Dt + f\mathbf{k} \times \mathbf{u} = -\nabla p/\rho_0 + \nabla \cdot \boldsymbol{\tau}_H + \partial \boldsymbol{\tau}_V/\partial z \tag{25}$$

and

$$\partial p/\partial z = \rho_w g \tag{26}$$

where ρ is water density, ρ_0 is a constant reference density, and $\boldsymbol{\tau}_H$ and $\boldsymbol{\tau}_V$ are horizontal and vertical components of the Reynold's stress tensor, respectively. The gradient operator ∇ describes variations in the two horizontal coordinates.

The water is assumed to be incompressible:

$$\nabla \cdot \mathbf{u} + \partial w/\partial z = 0 \tag{27}$$

Change in sea surface elevation η equals the vertical current w:

$$D\eta/Dt = (w)_{z=0} \tag{28}$$

Potential temperature T and salinity S satisfy

$$DT/Dt + \nabla \cdot \mathbf{q}_H + \partial(q_V + r)/\partial z = 0 \tag{29}$$

$$DS/Dt + \nabla \cdot \boldsymbol{\gamma}_H + \partial \gamma_V/\partial z = 0 \tag{30}$$

where r is absorbed solar radiative heat flux, a small term for the roughly week-long forecasts of interest here. At the surface, r equals the longwave radiation from the ice and atmosphere, weighted by the ice compactness. Penetration into the water follows *Roberts et al.* [1980]. The *Chen and Millero* [1976] equation of state relates density variations to temperature, salinity, and pressure.

Vertical components of Reynold's stress $\boldsymbol{\tau}_V$, heat flux $\mathbf{q}_V$, and salinity flux $\boldsymbol{\gamma}_V$ are

$$\boldsymbol{\tau}_V = K_V \, \partial \mathbf{u}/\partial z \tag{31}$$

$$\mathbf{q}_V = -\beta_T K_V \, \partial T/\partial z \tag{32}$$

$$\boldsymbol{\gamma}_V = -\beta_S K_V \, \partial S/\partial z \tag{33}$$

where K_V is vertical eddy viscosity and β_T and β_S are inverse Prandtl numbers that relate diffusion to viscosity. Material parameters in the ocean dynamics model match values presented by *Roberts et al.* [1980] and *Roberts and Seftor* [1981].

It is essential to estimate the vertical eddy diffusivity accurately, in order to describe the development of the mixed layer near the ice edge. We have chosen to use the level-two model of *Mellor and Yamada* [1974, 1977] as modified by *Martin* [1976], wherein

$$K_V = l^2(z)|\partial \mathbf{u}/\partial z|(1 - R/R_c)^{3/2} \qquad 0 \le R \le R_c \tag{34}$$

where l is turbulent length scale (assumed to be 0.3 times the Ekman length), $|\partial \mathbf{u}/\partial z|$ is vertical shearing deformation rate, R is Richardson number, and R_c is critical Richardson number. In a strict sense, this model is valid only for melting conditions where the Richardson number is positive. Under freezing conditions, salt is rejected, mixing downward until the density is uniform. The model approximates this process by a negative Richardson number and large eddy viscosity. Therefore the uniform density is approached asymptotically. This formulation appears valid, but the model has not been tested under freezing conditions.

In the open ocean, turbulent length scale is proportional to the Ekman depth, and uniform through the water column. Under the ice it approaches zero near the surface, which generates the observed log layer. We use an analytical solution [*McPhee*, 1982, 1983] to describe the vertical profiles in current velocity, temperature, and salinity in this layer.

Horizontal components of Reynold's stress $\boldsymbol{\tau}_H$, heat flux $\mathbf{q}_H$, and salinity flux $\boldsymbol{\gamma}_H$ are

$$\boldsymbol{\tau}_H = K_H \mathbf{D} \tag{35}$$

$$\mathbf{q}_H = -\beta_T K_H \nabla T \tag{36}$$

$$\boldsymbol{\gamma}_H = -\beta_S K_H \nabla S \tag{37}$$

where $\mathbf{D}$ is the two-dimensional velocity strain and K_H is horizontal eddy viscosity (which depends on horizontal grid spacing [*Smagorinsky et al.*, 1965].

6. Boundary and Initial Conditions

6.1. *Atmospheric Forcing*

The 10-m wind velocity $\mathbf{U}_{10}$ is determined by multiplying the geostrophic wind by 0.80 and turning its direction toward the left by 30°. Air stress acting on the ice $\boldsymbol{\tau}_{ai}$ is

$$\boldsymbol{\tau}_{ai} = \rho_a C_{ai} U_{10} \mathbf{U}_{10} \tag{38}$$

where ρ_a is air density and C_{ai} is a drag coefficient. Air stress acting on the ocean surface $\boldsymbol{\tau}_{aw}$ is

$$\tau_{aw} = \rho_a C_{aw} U_{10} \mathbf{U}_{10} \tag{39}$$

where C_{aw} is a drag constant. Both C_{ai} and C_{aw} were set to the nominal value of 0.003 for the MIZEX simulation (section 8). For the COST well simulation (section 9), the off-ice wind component was increased by 10% at nodes lying along the ice edge and the adjacent line of nodes. This modification was applied only to the air stress acting on the ice τ_{ai}, not to air stress acting on the water τ_{aw}, an empirical attempt to match the observations of *Reynolds* [1984] and *Overland et al.* [1983]. Similarly, the drag coefficient C_{ai} was increased by 50%. These increases better reflect the observation that ice drifts at nearly 5% of the wind speed at the ice edge, as opposed to 3% in the interior.

6.2. *Interface Conditions*

When the ocean surface is only partially covered by ice, the fluxes of heat and salt, and the water stress are linear combinations (weighted by compactness) of the corresponding terms from the air and ice. Traction acting on the ocean surface τ_w is a linear combination of air stress τ_{aw} acting directly on the ocean surface and water stress $\tau_{iw}(= -\tau_{wi}$, where τ_{wi} is the traction acting on the ice from the water) acting on the ocean surface from the bottomside of the ice:

$$\tau_w = (1 - A)\tau_{aw} + A\tau_{iw} \tag{40}$$

Traction acting between the ice and water is taken as a quadratic function of ocean current velocity at a depth of 2 m ($\mathbf{u}_2$) relative to the ice velocity ($\mathbf{v}$):

$$\tau_{wi} = \rho_w C_w |\mathbf{u}_2 - \mathbf{v}|(\mathbf{u}_2 - \mathbf{v}) \tag{41}$$

where ρ_w is water density and $C_w = 0.016$ is a drag coefficient [*Pease and Overland*, 1984].

Heat flux from the water to the ice Q_w is estimated as an average over a 10-m layer [*Large and Pond*, 1982; *Macklin*, 1983]:

$$Q_w = C_q \rho_w c_p V_r (T_r - T_{rf}) \tag{42}$$

where $C_q = 4 \times 10^{-4}$ is the heat transfer coefficient taken from *Josberger* [1987], ρ_w is water density, c_p is specific heat at constant pressure, V_r is ice speed relative to the 10-m current, T_r is ocean temperature, and T_{rf} is freezing temperature, both at 10-m depth. Relative speed V_r is a measure of the turbulence.

6.3. *Far-Field Boundary Conditions*

At the ice edge, traction $\mathbf{t} = \boldsymbol{\sigma}\mathbf{n}$ is zero. A similar assumption is made at the Bering Strait, for convenience. Along coastlines (including islands), ice velocity is zero, except for St. Matthew Island, which has been neglected completely in the two simulations presented here. Although the ice often slides along the coast in shear, this boundary condition is acceptable because the plasticity law allows the ice to fail in shear and the thickness distribution accounts for open water formed if ice retreats from shore.

When freezing occurs at the ice edge, $G(0, \mathbf{x}_e, t) = 1.0$, which provides a supply of infinitesimally thin ice to maintain the correct thickness distribution. At the Bering Strait, ice conditions are assumed uniform to determine ice influx.

Bering Sea simulations have used the ocean grid shown in Figure 3 that encompasses the entire Bering Sea. The intent was to locate the ocean boundaries far enough away from the region of interest that boundary conditions would have little effect on the desired solutions. Ocean current has been neglected in the Bering Strait and the Aleutian chain. At the ocean floor, current velocity, heat, and salt flux are zero.

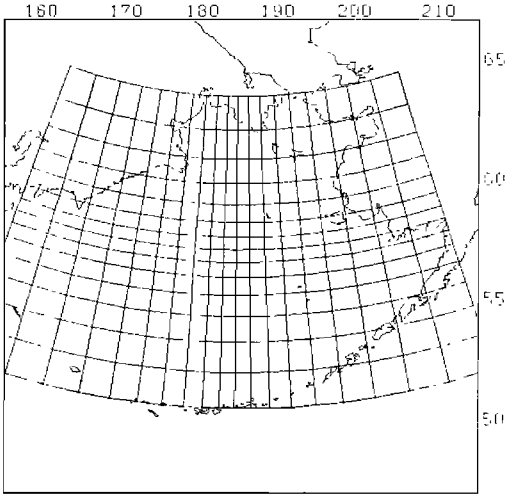

Fig. 3. Ocean model horizontal grid.

6.4. *Initial Conditions*

The initial ice thickness distribution profile is similar to that of *Wadhams and Horne* [1978] for the Arctic basin, except that concentration and median ice thickness are reduced for the Bering Sea ice. Estimates of ice concentration, type, and thickness were found in the Navy/NOAA Joint Ice Center (JIC) maps.

The initial ocean temperature distribution approximates the two-layer profile observed by *Muench and Schumacher* [1985]. In the open water south of the ice, surface temperature is derived from available sea surface temperature (SST) imagery, and mixed layer depth is set to a constant value. Under the pack ice, temperature is assumed to be horizontally and vertically uniform and at the freezing point. Within the marginal ice zone, the mixed-layer profile observed by *Muench and Schumacher* [1985] was used. A similar approach is used to specify the salinity. Surface and bottom salinity are assumed to be reasonable values (not measured) for regions outside the MIZ.

From the assumed initial temperature and salinity distributions, the model is "spun up" to determine ocean and ice velocities. Monthly average wind stress and barometric pressure field are applied until the velocities reach a quasi-steady state.

7. NUMERICAL SOLUTION METHODS

The ice model is approximated in conservative form by difference equations on a set of irregular quadrilaterals with rectangular connectivity (Figure 2). The difference equations are based on the leap-frog scheme, which alternates between ice velocity and stress. The scheme is explicit, except that time-centered water stress and Coriolis acceleration terms couple the two momentum equations. The time step is restricted by the Courant Friedrichs Lewy stability condi-

tion (the time step is limited to about 10 min for 50-km grid cells when strength is 10^4 N/m and elastic strains are limited to 0.1%). This small time step is acceptable because each explicit time step is fast, requiring no solutions of large sets of simultaneous equations. For problems where the internal stress is not important, ice strength may be assumed zero to avoid this restriction completely. The thickness distribution is integrated along the thickness-time characteristics, using a Runge-Kutta second-order scheme. The finite difference equations for a Lagrangian description are presented by *Pritchard and Colony* [1976]. For non-Lagrangian grid points, advection is calculated using an upwind approximation.

The ocean model is approximated in conservative form by difference equations on a fixed and regular latitude/longitude grid (Figure 3). The ocean depth is transformed to a σ coordinate, which varies logarithmically from zero at the surface to 1 at the bottom. Therefore the ocean mesh is refined near the surface. To avoid truncation errors in horizontal gradients, pressure is replaced by its difference from a reference pressure profile. The variables are staggered on the Arakawa B grid [*Roberts et al.*, 1980]. The time difference approximations are primarily leap-frog [*Roberts and Seftor*, 1981]. An alternating-direction implicit scheme stabilizes the momentum and temperature/salinity equations, while conditioning operators damp the high-frequency surface and internal wave oscillations. This scheme allows large time steps to be taken (we usually use time steps of 3 hours).

The ocean and ice models are coupled explicitly, with each time step of the ocean model using a known state of the ice. Similarly, the ice model assumes a known constant state of the ocean during each of its time steps. The ice model may take many time steps during one ocean model step, so the state of the ocean is interpolated linearly during the ice model time steps. Although the models are only explicitly coupled, we have observed no instabilities for 6-hour time steps of the ocean model. A 9-day simulation using step sizes of 3 hours on a 21 × 16 × 10 ocean grid and a 32 × 21 × 6 ice grid requires about 4 hours of CPU on a PRIME 750 computer (the PRIME 750 runs at about one-thirtieth the speed of the CRAY1).

8. MIZEX-WEST VALIDATION

Ice conditions were simulated for February 18–27, 1983, when the MIZEX-West field program was conducted [*Cavalieri et al.*, 1983]. Concurrent observations of ocean, atmosphere, and ice behavior during this period provided accurate data for initializing and driving the model and for testing its performance.

8.1. *Input Data*

Digitized barometric pressure, air temperature, relative humidity, wind velocity components, geopotential height, and SSTs were obtained from the National Center for Atmospheric Research (NCAR) on a 2.5° longitude/latitude grid two times per day. Typical winds in the test region had a northerly component, which caused the ice cover to be driven steadily southward into warmer waters. In addition, ocean temperature and salinity profile data [*Muench and Schumacher*, 1985] established initial ocean conditions in the MIZ. These initial conditions were extrapolated uniformly along the entire lateral extent of the ice edge.

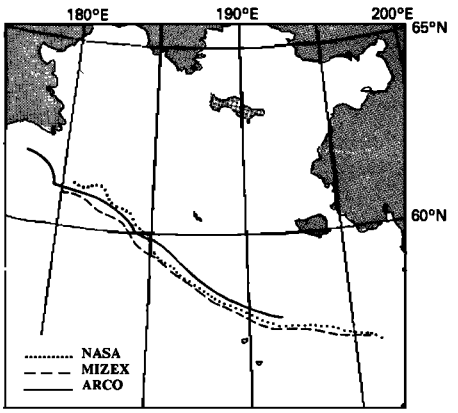

Fig. 4. Ice edge on February 20, 1983, observed by three different sources.

Ice data were assembled from a variety of sources, including JIC, ARCO, MIZEX, and NASA. Initial ice concentration and thickness distribution were derived from an ice map for February 19, 1983 [*Cavalieri et al.*, 1983]. A combination of ice maps from the Navy/NOAA Joint Ice Center (JIC) and from a private source (ARCO) defined the initial ice edge location. *Overland and Pease* [1983] described ice conditions (from MIZEX) using aircraft and satellite data. Finally, D. J. Cavalieri (NASA, personal communication, 1985) provided a map of ice edge location for several days of the simulation interval.

No single source of ice data covered the entire interval; there were days when only one or two of the sources provided data, and days when only a segment of the ice edge was identified. The various sources often agreed poorly among themselves. For instance, Figure 4 shows the ice edge location according to three different sources on February 20, 1983. Near 190°E, they agree fairly well, to within roughly 20 km, but near 182°E, the largest separation was about 60 km. Therefore, comparing predicted ice edge locations with observations from different sources may produce uncertainty as large as model errors. Since the ice edge from the Soviet Union to 190°E was initialized with ARCO data, ice edge comparisons were made only against the ARCO data, and these were limited to the western Bering from 180° to 190°E where the best set of ice edge locations was available.

8.2. *Results*

This discussion is limited to ice edge location and ice velocity. Figure 5 shows observed ice edge location on February 18 and 27, and simulated ice edge location on February 22, 23, 24, and 27 (last day of simulation). In the central and western Bering Sea the ice edge moved rather far southwestward, but there was far less movement in the eastern Bering Sea. Near 60°N, 185°E, the ice edge advanced about 115 km in 11 days. In the western Bering, thicker ice from the north is advected southward, and since it took longer to melt, the ice edge advanced further than in the eastern Bering, where thinner ice existed to the north. The ice edge advanced farther during February 22–24 than at any

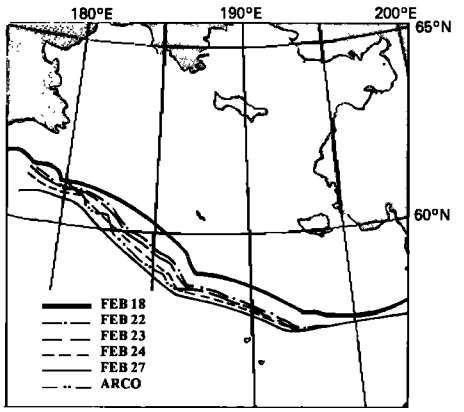

Fig. 5. Ice edge simulated for February 18–27, 1983. The February 18 line determined initial position (observed). The ARCO line was observed on February 27.

other time, apparently because of the higher wind speeds at that time.

As the ice edge moved into open water, ice melted and the mixed layer developed to a depth of about 50 m, consistent with observations of *Muench and Schumacher* [1985]. At this depth, the eddy viscosity approached zero, preventing deeper transfer of momentum, heat, and salt, and allowing sharp gradients to persist. The ratio of kinetic energy input by the wind to potential energy input by melting (buoyancy) controlled the thickness of this layer. It rarely exceeded 100 m, and momentum input at the surface tended to be confined to the thickness of the mixed layer. In contrast, no such density barrier developed in a simplified model in which the eddy viscosity was a constant, independent of the Richardson number. In the constant eddy viscosity model, momentum diffused throughout the water column. Intuitively, it would seem that ice over the strong pycnocline should move further than ice over a vertically uniform ocean because the energy input from the wind would be confined to a shallower layer. This idea was tested by a model in which temperature and salinity were constant, eddy viscosity was retained, and the Richardson number was set to zero. This allowed the development of a surface Ekman layer but no buoyancy barrier due to melting (constant temperature and salinity). The ice edge advanced about 170 km for this model, which was significantly greater than the 115 km predicted by the complete model. This apparent paradox can be explained by the generation of turbulence in the mixed layer and its effects on vertical heat transfer, which is discussed below.

Ice velocities and ice edge velocities tabulated for a grid point southwest of St. Matthew Island are shown in Table 1. The average ice floe velocities predicted by the model over the simulation interval and by the simplified version were 36 and 34 cm/s, respectively. However, the corresponding average ice edge velocities were 14 and 22 cm/s, which suggested that the meltback rate was smaller for the simplified model. Velocity in the mixed layer was influenced primarily by the balance between the Coriolis and the turbulent viscous forces where the eddy viscosity was a function of both the kinetic (velocity shear) and potential (buoyancy) energy. At the depth where buoyancy dominated, the eddy viscosity dropped to zero. This inhibited the transfer of heat and momentum, and a well-mixed, fast moving surface layer developed which was fresher and colder than the underlying water. Since the velocity shear within this layer was large, turbulent heat flux transferred heat for melting ice and increased the meltback rate, which more than compensated for the increased ice velocities.

The model simulation also produced a westward component of ocean current in the MIZ. *Muench and Schumacher* [1985] observed this along-edge flow and attributed it to the horizontal density gradient set up perpendicular to the ice edge by melting. This along-edge flow reduced ice edge advance by increasing the turbulence levels (and the heat flux) slightly, and turning the ice velocity rightward near the ice edge. Figure 6 shows the quasi-steady baroclinic surface current simulated with the initial density field but no other driving forces.

Daily ice speeds and directions derived from the movement of MIZEX buoy 3 during February 19–27, 1983, are shown in Table 1, which also includes model output for a nearby grid point. The simulated average daily ice velocity of 36 cm/s agrees well with the observed buoy motion of 38 cm/s. The simulated average direction of buoy movement of 225° clockwise from true north equals the observed value. The accurate simulation of ice drift velocity suggests that the parameterization of the winds and the drag coefficients is accurate.

TABLE 1. Daily Average Values of Simulated and Observed Ice Floe and Ice Edge Speed (cm/s) and Direction (Degrees Clockwise From North) at a Location Slightly Southwest of St. Matthew Island

	Speed, cm/s			Direction, °T		
	Ice			Ice		
Day in February	Model	MIZEX Buoy 3	Ice Edge Model	Model	MIZEX Buoy 3	Ice Edge Model
19	42	34	13	235	220	210
20	36	34	13	200	215	205
21	27	32	11	205	210	205
22	35	34	16	200	215	205
23	42	45	17	210	220	210
24	56	50	21	225	225	210
25	27	45	9	235	235	210
26	34	39	15	245	235	210
27	25	30	8	255	230	210
Average	36	38	14	225	225	210

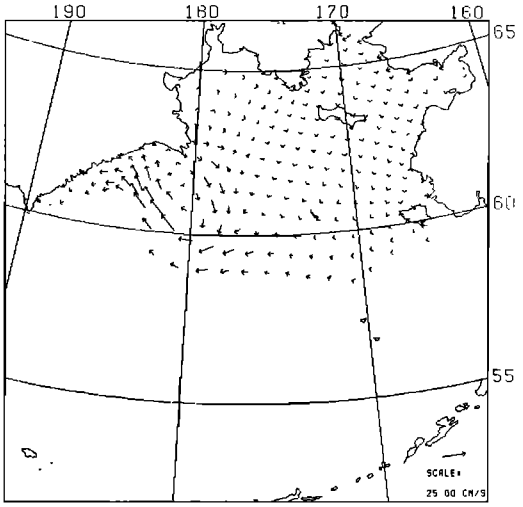

Fig. 6. Quasi-steady baroclinic surface current field.

Simulated ice edge positions are also compared with observed positions. Figure 7 shows ice edge position on February 27, at the end of the simulation period. Both MIZEX and ARCO data appear on the charts, but only the ARCO position data were used for quantitative comparisons. The model overestimated the total advance of the ice edge by about 24 km, an average of about 3 km/d. The model underestimated the advance of a 250-km-wide segment of the ice edge near 180°–185°E longitude by about 9 km for the February 19–21 interval. Since the predicted ice floe velocities agreed with observed buoy movements, this error suggested that the model melt rates were too high. For February 22 the simulated advance was 16 km, giving a net overestimation of 7 km over the first four days of the simulation. The error early in the simulation was due primarily to errors in initializing the simulation. An error of 17 km over the last five days of the simulation was well within the limits of observational uncertainties.

9. COST Well Validation

During the first two weeks of January 1983, a consortium of petroleum companies drilled a COST well on the north Aleutian shelf [*Grittner et al.*, 1983]. As with the MIZEX-West time period, concurrent observations of ocean, atmosphere, and ice behavior during this period provided accurate data for initializing and driving the model, and for testing its performance.

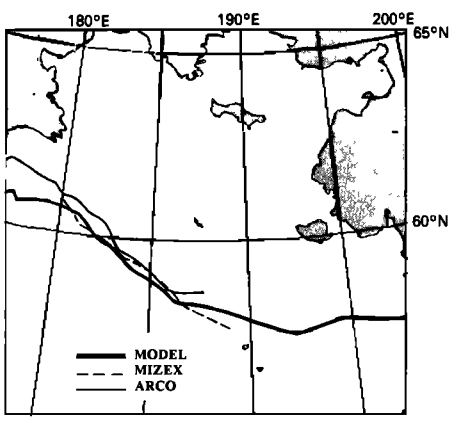

Fig. 7. Simulated and observed ice edge on February 27.

9.1. *Input Data*

As in the MIZEX-West simulation, NCAR data were used to define the barometric pressure and the initial sea surface temperature fields. During this 2-week period, northerly and northeasterly winds up to 20 m/s persisted. However, they diminished rapidly toward the west, where a high-pressure system remained nearly stationary over the middle of the Bering Sea. Comparison of the NCAR data to locally enhanced barometric pressure fields showed some large errors in regions where the meteorological fields have steep spatial gradients. The transition, as shown by the NCAR data, from weak winds in the central Bering Sea to strong winds in the east was not as rapid as that determined in the locally enhanced analysis. In addition, the NCAR wind patterns were shifted to the east compared with enhanced winds.

Air temperatures at the drill site ranged from 2° to −12°C, but farther north near the coast of Alaska, the temperatures were much colder (at Bethel, the average daily temperatures ranged from −17° to −28°C). Ice upwind of the drill site was subjected to these cold temperatures by the offshore winds. NCAR data were 6°–9°C warmer than observed temperatures.

The ice edge location was monitored daily by aircraft using side-looking airborne radar. *Shapiro* [1984] studied the edge movement and ice motions and showed that substantial melting occurred at the ice edge where individual floes moved rapidly to the south, but the ice edge advanced slowly or not at all.

9.2. *Results*

Figure 8 shows the movement of the ice edge for the period January 6–12, 1983 [*Shapiro*, 1984]. The most prominent feature is the development of the large bulge that extended toward the COST well (identified by a star), with very little movement in Bristol Bay or west of 190°E. In addition, there was a persistent open-water area south/southeast of Cape Nevenham. Daily displacements of individual floes (identified in the imagery) are also shown. The floes in the developing bulge were moving at speeds ranging from 40 to 60 cm/s. The ratio of ice floe speed to surface wind speed was generally about 3% but increased near the ice edge to about 5%. Several simulations were performed to determine the effects of the large wind gradients and of errors in the winds and air temperatures. We learned that the wind gradient and low overland air temperature could explain much of the bulge that developed in the ice edge.

Figure 9 presents simulated and observed ice edge locations on January 10. The simulated ice trajectory of one point from January 4–9 is superposed. It reached the ice edge on January 9 and melted. The comparison between simulated and observed ice edge location was similar throughout the time period. The simulated ice velocity normal to the ice edge ranged from 30 to 60 cm/s in the bulge, while ice edge velocities elsewhere ranged from −5 (retreat) to 30 cm/s. The direction of ice motion was turned more toward the east than observed (see Figure 8), but the speeds compared reasonably well. The bulge advanced about 175 km over the 9-day simulation period. The simulation error in the ice edge

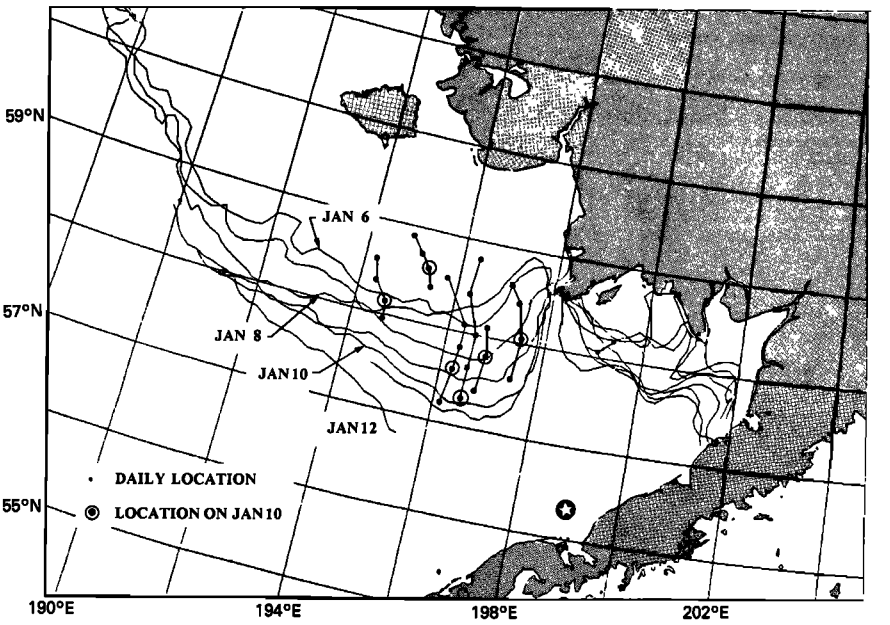

Fig. 8. Observed ice edge during January 6–12, 1983 [from *Shapiro*, 1984].

location, west of Cape Nevenham, varied from 0 to 50 km, which was about 30% of the total bulge advancement. The simulated thickness distribution south of Nunivak Island changed substantially during the first three days of the 9-day simulation period, which suggested that our initial conditions were inaccurate. Farther from shore, this problem was not apparent. The simulated fraction of area covered by open water and new ice on January 10 is presented in Figure 10. Larger fractions appear along lee shores where ice was advected away and new ice froze, and along the ice edge where the ice melted. These were reasonable results, but we lacked data to make a quantitative comparison.

In Bristol Bay the winds were stronger than they were SSW of Cape Nevenham, but the ice edge did not advance far. It appears likely that although these cold northerly winds increased the freezing rate, ice formed near this lee coast was advected south to the ice edge in about 2 days, where it melted in warm waters. There was not time to grow ice thicker than 10–20 cm. On the other hand, ice formed near Nunivak Island had about 6 days in persistent 15 m/s winds to reach warm water. In the cold air off the coast of Nunivak, ice grew up to 40 cm thick before beginning to melt. Therefore the ice edge tended to advance farther to the southwest of Cape Nevenham simply because the thicker ice took longer to melt (note that it is unlikely for ice formed near Nunivak to drift into Bristol Bay).

The ice growth hypothesis can explain the differences in

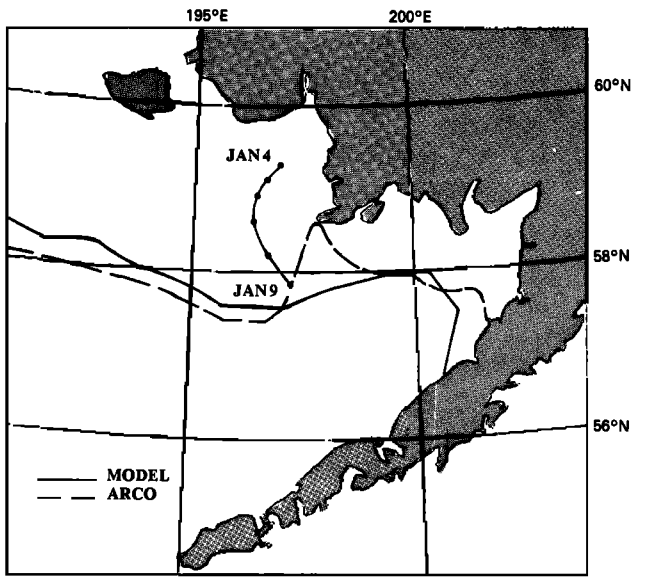

Fig. 9. Simulated and observed ice edge on January 10. The dotted line is a simulated ice floe trajectory from January 4–9, when it melted.

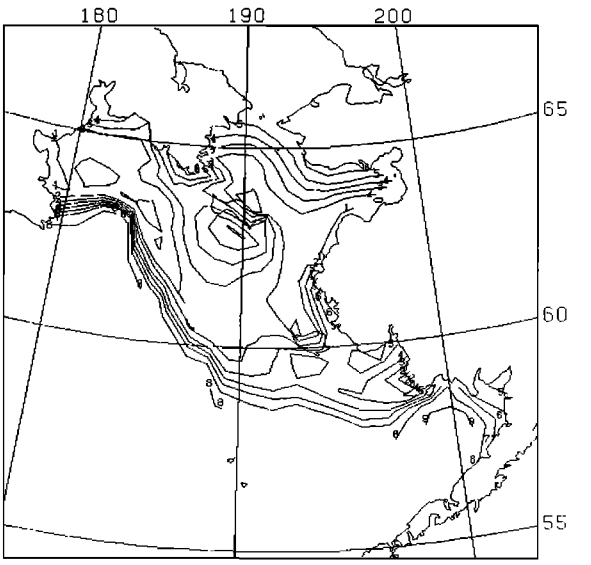

Fig. 10. Distribution of thin ice on January 10. Contours represent the number of tenths of coverage of ice thinner than 20 cm thick.

the ice edge movement between Bristol Bay and areas to the immediate west but not the smaller advance observed SSW of Nunivak. There the rapid drop in wind speed reduced the ice drift velocity and therefore the ice edge velocity.

South of Cape Nevenham, the persistent open water region was probably caused by warm water flowing northward through Unimak pass, along the Aleutian chain, through Bristol Bay, and along the coast.

While many investigators claim that ice is never found in waters above 1°C, we must be careful when using this rule of thumb for determining ice advance. This observation does not mean that ice cannot extend past the point where 1°C water is located. Ice could drift into warm water and cool it, thereby moving the 1°C isotherm and blur the distinction between cause and effect. Does the 1°C water melt the ice, or does the ice cool the water to below 1°C? Experience with the model shows that, regardless of the initial SST at the ice edge, the edge seems to "seek" an equilibrium temperature of near −0.5° to −1.0°C. Warm ocean temperatures seaward of the MIZ do inhibit ice edge advance. For instance, a point 100 km in front of the ice edge in 4°C water is much less likely to be overrun by ice during a given time period than if it were in 1°C water.

The model showed that ice edge motion was quite sensitive to the ocean surface current. This dependence may be explained by solving (20) for ice edge velocity and expressing the ice velocity as the sum of current $\mathbf{c}$ and ice velocity relative to the current $\mathbf{v}_r$

$$\partial \mathbf{x}_e/\partial t = \mathbf{c} + \mathbf{v}_r - M\mathbf{n} \tag{43}$$

The meltback rate depends on the mixed layer turbulence, which is a function of $\mathbf{v}_r$. The ice velocity relative to current $\mathbf{v}_r$ depends on the local wind [e.g., *Pritchard*, 1988]. When winds are off-ice, these two terms tend to oppose and cancel each other, which makes the ice edge velocity more strongly dependent on the current $\mathbf{c}$.

10. CONCLUSION

A coupled atmosphere-ice-ocean dynamics model has been successfully developed. The purpose of this model is to support offshore drilling operations by providing 5- to 7-day ice forecasts. The ice dynamics model is based on an extended version of the AIDJEX elastic-plastic constitutive law with ice conditions described by the thickness distribution. The ocean model is based on the SIGMA code, an N layer, primitive equation model that includes both barotropic and baroclinic flows. Thermal energy and mass budgets are included to describe the temperature and salinity changes that accompany the melt or growth of ice.

The ice edge location is prescribed, and its motion is described directly by accounting for both the drift and melt (or growth) of ice floes there. The ice behavior is described in terms of a referential description using an adaptive grid that follows the ice edge, that is Eulerian around islands and certain other areas, that is Lagrangian in still other areas, and that makes smooth transitions in between. This grid motion, which may be modified by the user, provides a means of resolving ice conditions to within about 5 km near the ice edge, while reducing the number of grid cells needed for numerical calculations.

The model has been used to simulate the ice conditions during the 1983 MIZEX-West field program and during drilling operations of the 1983 north Aleutian COST well. These simulations have allowed us to evaluate the model performance by comparing the modeled ice-ocean behavior with observed ice motions, ice and ocean conditions, and ice edge motions. Material properties were set to nominal values from the literature. In the two simulations, the ice edge motion has been described to within about 5 km/d.

The simulations showed that the motion of the ice edge from day to day depended equally on the ice drift due to winds and currents and on the melting of ice floes as the ice edge drifted into warmer water. The model correctly described the evolution of the mixed layer as fresh water due to melting ice was subsequently mixed downward by the turbulence. The model showed that increasing the ice drift speed also increased the meltback rate because of the associated higher turbulent heat flux, and therefore increased drift speeds did not necessarily result in significantly more rapid advance of the ice edge. Baroclinic flows generated by the density gradient across the ice edge were also correctly described by the model.

The tests showed that it is important to enhance the large-scale data fields (available from data banks and services) of barometric pressure, air temperature, sea surface temperature, and ice conditions by including local observations or data from specialized local analyses. Data near the ice edge, in the open waters in front of the ice edge, and ice and weather conditions well behind the ice edge all are important for accurate forecasting.

Although the model is large and complex, its development has proceeded with the requirement kept firmly in mind that it is to be used to make frequent (at least daily) forecasts of ice edge location and ice conditions during drilling operations. We have attempted to describe each of the essential processes completely, yet simply, so that the model behaves accurately under the full range of driving forces and environmental conditions. And, with today's powerful minicomputers, this model can make a real-time ice forecast for the Bering Sea within an hour. On bigger, more powerful machines, this time can be reduced to a few minutes.

A complex set of processes governs the formation, movement, and melting of ice in the Bering Sea. Also, melting at the ice edge alters the local hydrographic structure and circulation of the ocean, which in turn provides feedback to the melting process. The relative importance of these processes varies at different times and locations, which is the reason for developing a model that includes each of the basic processes and allows the numerical scheme to determine the composite solution. While this model was developed to serve as a short-term ice forecasting tool for Bering Sea drilling operations, it is also applicable elsewhere. The same set of physical processes occurs in the Greenland Sea and in the Chukchi Sea in spring and fall. Although the different processes have more or less importance in the other regions, they remain relevant, and since the model itself determines the relative importance of the processes as a result of the driving forces, it can be applied equally well in these, and other, MIZ regions.

Acknowledgments. The authors sincerely thank ARCO Oil and Gas Company for its support of this research study and permission to publish this description of the model, and Mobil Research and Development Corporation for support during the first phase. This study was performed while the first three authors were employed by

Flow Industries, Inc., and we appreciate the continued help of D. C. Echert and K. L. Hammond in preparing this manuscript. The help and support of several other individuals are also acknowledged. All of these scientists and engineers helped in a variety of ways, and we can only describe the main role played by each. W. Spring, MRDC, conceived the project and, along with D. B. Reed, ARCO, guided its first phase. T. M. Mitchell, ARCO, gave physical oceanography technical advice throughout. J. Karish, ARCO, ensured continued funding. D. R. Thomas, formerly of Flow, helped write the ice dynamics code. J. C. Schedvin identified the essential oceanographic physics and selected the code to model it, and sadly, must be acknowledged posthumously. L. H. Shapiro provided data and interpretation of observed behavior during the COST well operations. Finally, M. G. McPhee, O. M. Phillips, and G. O. Roberts served as consultants on physical oceanography and ocean modeling.

REFERENCES

Cavalieri, D. J., et al., MIZEX-West: Bering Sea Marginal Ice Zone Experiment, *Eos Trans. AGU, 64*(40), 578–581, 1983.

Chen, C. T., and F. J. Millero, The specific volume of seawater at high pressures, *Deep Sea Res., 23*, 595–612, 1976.

Coachman, L. K., and K. Aagaard, Re-evaluation of water transports in the vicinity of Bering Strait, in *The Eastern Bering Sea Shelf: Oceanography and Resources*, vol. 1, edited by D. W. Hood and J. A. Calder, pp. 95–110, Government Printing Office, Washington, D. C., 1981. (Available from University of Washington Press, Seattle.)

Coon, M. D., G. A. Maykut, R. S. Pritchard, D. A. Rothrock, and A. S. Thorndike, Modeling the pack ice as an elastic-plastic material, *Aidjex Bull. 24*, pp. 1–106, Univ. of Wash., Seattle, 1974.

Dixit, B. C., G. R. Pilkington, and F. J. Eley, Environmental and performance monitoring for offshore Arctic exploration structures, paper presented at the Arctic Offshore Technology Conference, Calgary, Canada, Nov. 6–9, 1984.

Eley, F. J., Ice monitoring and forecasting for the Beaudril "Kulluk," Proceedings of the Canadian East Coast Workshop on Sea Ice, *Can. Tech. Rep. Hydrogr. Ocean Sci.*, no. 73, 598–614, 1986.

Grittner, S. F., J. M. Karish, and R. A. Steward, The surveillance program to support the north Aleutian shelf COST well no. 1, *POAC 83*, pp. 282–296, Tech. Res. Cent. of Finland, Espoo, 1983.

Hibler, W. D., III, Numerical modeling of sea ice dynamics and ice thickness characteristics, *CRREL Rep. 85-5*, Cold Reg. Res. and Eng. Lab., Hanover, N. H., 1985.

Hughes, F. W., L. K. Coachman, and K. Aagaard, Circulation, transport and water exchange in the western Bering Sea, in *Oceanography of the Bering Sea*, edited by D. W. Hood and E. J. Kelley, pp. 59–98, University of Alaska Press, Fairbanks, 1974.

Josberger, E. G., Sea ice melting in the marginal ice zone, *J. Geophys. Res., 88*, 2841–2844, 1983.

Josberger, E. G., Bottom ablation and heat-transfer coefficients from the 1983 Marginal Ice Zone Experiments, *J. Geophys. Res., 92*(C7), 7012–7016, 1987.

Kinder, T. H., and J. D. Schumacher, Circulation over the continental shelf of the southeastern Bering Sea, in *The Eastern Bering Sea Shelf: Oceanography and Resources*, vol. 1, edited by D. W. Hood and J. A. Calder, pp. 53–75, U.S. Government Printing Office, Washington, D. C., 1981. (Available from University of Washington Press, Seattle.)

Kollé, J. J., and R. S. Pritchard, A comparison of two sea ice trajectory models with AIDJEX observations, *J. Energy Resour. Technol., 105*(3), 346–351, 1983.

LaBelle, J. C., J. L. Wise, R. P. Voelker, R. H. Schulze, and G. M. Wohl, *Alaska Marine Ice Atlas*, Arctic Environmental Information and Data Center, University of Alaska, Anchorage, 1983.

Large, W. G., and S. Pond, Sensible and latent heat flux measurements over the ocean, *J. Phys. Oceanogr., 12*, 464–482, 1982.

Macklin, S. A., Wind drag coefficient over first-year sea ice in the Bering Sea, *J. Geophys. Res., 88*(C5), 2845–2852, 1983.

Martin, P. J., A comparison of three diffusion models of the upper mixed layer of the ocean, *NRL Memo. Rep. 3399*, Nav. Res. Lab., Washington, D. C., 1976.

Martin, S., and J. Bauer, Bering Sea ice-edge phenomena, in *The Eastern Bering Sea Shelf: Oceanography and Resources*, vol. 1, edited by D. W. Hood and J. A. Calder, pp. 189–212, U.S. Government Printing Office, Washington, D. C., 1981. (Available from University of Washington Press, Seattle.)

Maykut, G. A., Energy exchange over young sea ice in the central Arctic, *J. Geophys. Res., 83*(C7), 3646–3658, 1978.

Maykut, G. A., Large-scale heat exchange and ice production in the central Arctic, *J. Geophys. Res., 87*(C10), 7971–7984, 1982.

McPhee, M. G., Sea ice drag laws and simple boundary layer concepts, including application to rapid melting, *CRREL Rep. 82-4*, Cold Reg. Res. and Eng. Lab., Hanover, N. H., 1982.

McPhee, M. G., Turbulent heat and momentum transfer in the oceanic boundary layer under melting pack ice, *J. Geophys. Res., 88*, 2827–2835, 1983.

Mellor, G. L., and T. Yamada, A hierarchy of turbulence closure models for planetary boundary layers, *J. Atmos. Sci., 32*, 1791, 1974.

Mellor, G., and T. Yamada, A turbulence model applied to geophysical fluid problems, in *Proceedings of the Symposium on Shear Flow Turbulence*, pp. 6.1–6.14, Pennsylvania State University, University Park, 1977.

Muench, R. D., and K. Ahlnas, Ice movement and distribution in the Bering Sea from March to June 1974, *J. Geophys. Res., 81*, 4467–4476, 1976.

Muench, R. D., and J. D. Schumacher, On the Bering Sea ice edge front, *J. Geophys. Res., 90*(C2), 3185–3197, 1985.

Niebauer, H. J., Sea ice and temperature variability in the eastern Bering Sea and the relation to atmospheric fluctuations, *J. Geophys. Res., 85*, 7507–7515, 1980.

Overland, J. E., and C. H. Pease, Cyclone climatology of the Bering Sea and its relation to sea ice extent, *Mon. Weather Rev., 110*, 5–13, 1982.

Overland, J. E., and C. H. Pease, MIZEX-West, NOAA WP-3D research aircraft flight report, NOAA Pac. Mar. Environ. Lab., Seattle, Wash., 1983.

Overland, J. E., R. M. Reynolds, and C. H. Pease, A model of the atmospheric boundary layer over the marginal ice zone, *J. Geophys. Res., 88*, 2836–2840, 1983.

Pease, C. H., Eastern Bering Sea processes, *Mon. Weather Rev., 108*(12), 2015–2023, 1980.

Pease, C. H., Eastern Bering sea ice dynamics and thermodynamics, in *The Eastern Bering Sea Shelf: Oceanography and Resources*, vol. 1, edited by D. W. Hood and J. A. Calder, pp. 213–222, U.S. Government Printing Office, Washington, D. C., 1981. (Available from University of Washington Press, Seattle.)

Pease, C H., and J. E. Overland, An atmospherically driven sea-ice drift model for the Bering Sea, *Ann Glaciol., 5*, 111–114, 1989.

Pease, C. H., and S. A. Salo, Sea ice drift near Bering Strait during 1982, *J. Geophys. Res., 92*(C4), 7107–7126, 1987.

Pritchard, R. S., An elastic-plastic constitutive law for sea ice, *J. Appl. Mech., 42*(2), 379–384, 1975.

Pritchard, R. S., Mechanical behavior of pack ice, in *Mechanics of Structured Media*, part A, edited by A. P. S. Selvadurai, pp. 371–405, Elsevier, New York, 1981.

Pritchard, R. S., Norton Sound and northeastern Bering Sea ice behavior 1981–82, *OMAE 88*, vol. IV, pp. 69–74, Am. Soc. Mech. Eng., Houston, Tex., 1988.

Pritchard, R. S., and R. Colony, A difference scheme for the AIDJEX sea ice model, in *Numerical Methods in Geomechanics*, vol. II, edited by C. S. Desai, pp. 1194–1209, American Society of Civil Engineers, New York, 1976.

Reynolds, M., On the local meteorology at the marginal ice zone of the Bering Sea, *J. Geophys. Res., 89*(C4), 6515–6524, 1984.

Roberts, G. O., and J. L. Seftor, A sigma coordinate ocean forecasting computer code, II, Time representation and stability properties, *Rep. SAI-80-957-WA*, 82 pp., Sci. Appl., McLean, Va., 1981.

Roberts, G. O., J. L. Seftor, and W. J. Grabowski, A sigma coordinate ocean forecasting computer code, I, Model differential equations, spatial finite-difference representation and conservation properties, *Rep. SAI-80-956-WA*, 136 pp., Sci. Appl., McLean, Va., 1980.

Rothrock, D. A., The energetics of the plastic deformation of pack ice by ridging, *J. Geophys. Res., 80*(33), 4514–4519, 1975.

Shapiro, L. H., Growth and movement of the ice cover in the eastern Bering Sea, November 1982–January 1983, Geophys. Inst., Univ. of Alaska, Fairbanks, 1984.

Smagorinsky, J., S. Manabe, and J. L. Holloway, Jr., Numerical results from a nine-level general circulation model of the atmosphere, *Mon. Weather Rev.*, *93*(12) 727–768, 1985.

Steen, J. W., and J. D. Trobak, Dome-Canmar's operational ice forecasting system for the Beaufort Sea, Proceedings of the Canadian East Coast Workshop on Sea Ice, *Can. Tech. Rep. Hydrogr. Ocean Sci.*, no. 73, 615–650, 1986.

Takenouti, A. Y., and K. Ohtani, Currents and water masses in the Bering Sea: A review of Japanese work, in *Oceanography of the Bering Sea*, edited by D. W. Hood and E. J. Kelley, pp. 39–57, University of Alaska Press, Fairbanks, 1974.

Thompson, J. F. (Ed.), *Numerical Grid Generation*, North-Holland, Amsterdam, 1982.

Thorndike, A. S., D. A. Rothrock, G. A. Maykut, and R. Colony, The thickness distribution of sea ice, *J. Geophys. Res.*, *80*(33), 4501–4513, 1975.

Wadhams, P., and R. J. Horne, An analysis of ice profiles obtained by submarine sonar in the AIDJEX area of the Beaufort Sea, *Tech. Rep. 78-1*, Scott Polar Res. Inst., Cambridge, England, 1978.

Walsh, J. W., and C. M. Johnson, An analysis of Arctic sea ice fluctuations, 1953–77, *J. Phys. Oceanogr.*, *9*, 580–591, 1979.

Zillman, J. W., A study of some aspects of the radiation and heat budgets of the southern hemisphere oceans, *Meteorol. Stud. 26*, Bur. of Meteorol., Dep. of the Interior, Canberra, Australia, 1972.

D. J. Hanzlick, 7335 34th Avenue, N.E., Seattle,WA 98115.

A. C. Mueller, Flow Industries, Inc., 2144-68th Avenue South, Kent, WA 98032.

R. S. Pritchard, IceCasting, Inc., 11042 Sand Point Way, N.E., Seattle, WA 98125.

Y.-S. Yang, Arco Oil and Gas Company, 2300 West Plano Parkway, Dallas, TX 75221.

(Received July 11, 1988;
accepted July 5, 1989.)